AIAA 2004-4051

Higher Flowfield Approximations for Solid Rocket Motors with Tapered Bores

O. C. Sams, IV, J. Majdalani and G. A. Flandro
Advanced Theoretical Research Center
University of Tennessee Space Institute
Tullahoma, TN 37388

40th AIAA/ASME/SAE/ASEE Joint Propulsion Conference and Exhibit
11–14 July 2004
Fort Lauderdale, FL

40th AIAA/ASME/SAE/ASEE Joint Propulsion Conference and Exhibit
11-14 July 2004, Fort Lauderdale, Florida

AIAA 2004-4051

Higher Flowfield Approximations for Solid Rocket Motors with Tapered Bores

Oliver C. Sams IV,* Joseph Majdalani,† and Gary A. Flandro‡
University of Tennessee Space Institute, Tullahoma, TN 37388

Current ballistics analyses require detailed information regarding the key characteristics of the flowfields present in the combustion chambers of solid rocket motors. In this study, our purpose is to develop an internal flowfield applicable to circular-port solid rocket motors with tapered bores. Our analysis is based on the vorticity-stream function method, allowing one to resolve the resulting problem under isothermal, inviscid, rotational and steady-state conditions. Here, the approach employed in Clayton's original investigation of tapered motors is implemented with the aim of producing an approximate solution that reflects the behavior of the flowfield at higher orders as well as combined geometric configurations. In the advent of a nonlinear governing equation, an initial solution is sought with the use of regular perturbations. Additionally, an analytical solution is explored using the method of variation of parameters; its outcome will be shown to be identical to the leading order solution obtained by asymptotic analysis. In an effort to validate the approximations used throughout this work, a numerical simulation is performed and compared to the analytical results.

Nomenclature

F	=	momentum thrust
$\bar{p}$	=	dimensional pressure
p	=	normalized pressure, $\bar{p}/\rho V_b^2$
R_0	=	dimensional radius of cylindrical motor
$\bar{r}$	=	dimensional radial coordinate
r	=	normalized radial coordinate, $\bar{r}/R_0$
$\bar{u}$	=	dimensional velocity components, $(\bar{u}_z, \bar{u}_r)$
u	=	normalized velocity, $\bar{u}/V_b$
V_b	=	injection velocity at propellant surface
$\bar{z}$	=	axial coordinate
z	=	normalized axial coordinate, $\bar{z}/R_0$
β	=	velocity ratio, $u_{\max}/u_{\text{ave}}(x), u_{\max}/u_{\text{ave}}(z)$
ρ	=	density
η	=	coordinate transformation, $\eta = r^2$
ψ	=	normalized stream function
Ω	=	normalized vorticity

Subscripts

0	=	leading order, parallel chamber quantities
1	=	first-order correction
b	=	burning surface
r, z	=	radial or axial component
θ	=	azimuthal component

Superscript

–	=	dimensional quantity

I. Introduction

THE extraction of critical design parameters for solid rocket motors through internal ballistics analysis is fundamental in modern propulsion system design and development. Information regarding the flowfields generated in combustion chambers and the motor performance associated with them comprise the framework necessary to evaluate specific motor requirements, candidate grain geometries, motor configurations, and propellant formulations.[1] Ballistics analyses are available to predict chamber pressures, combustion instabilities, thrust, mass flux and grain burn rate histories based on the velocity and pressure profiles provided by the mean flowfield.[2-9] An increase in the accuracy of predictions provided by ballistics analyses would invariably require enhanced flowfield models.

*Graduate Research Associate, Marquette University, Department of Mechanical and Industrial Engineering. Member AIAA.

†Jack D. Whitfield Professor of High Speed Flows, Department of Mechanical, Aerospace and Biomedical Engineering. Member AIAA.

‡Boling Chair Professor of Excellence in Propulsion, Department of Mechanical, Aerospace and Biomedical Engineering. Associate Fellow AIAA.

In the past, several researchers have successfully developed mean flow models that have set the standard for current flowfield investigations. Among them is Culick,[10] whose original rotational, inviscid solution remains at the foundation of this work. Current research involves the evaluation of unsteady wave motions,[11-14] acoustic interactions with propellant burning,[15] velocity and pressure coupling,[16] nonlinear (DC) pressure shift,[17] triggering amplitudes,[18] limit cycle amplitudes,[19] as well as particle-mean flow interactions,[20-24] two-phase flow effects,[25] distributed combustion, parietal vortex shedding,[26-28] and both spatial and temporal instabilities of the mean flow.[29-32]

It is imperative that the rocket propulsion community continues to seek refinement in current analytical, numerical and experimental flowfield modeling methods in order to avoid economic losses resulting from adjusted mission requirements, over-design, mission failures and catastrophic accidents due to under and over-prediction of the pressure load in the motor case. Despite the advent of advanced propulsion concepts such as solar and magnetic sails, antimatter and electric arc propulsion, it remains of paramount importance to refine existing methods and models pertaining to the design and analysis of chemical propulsion systems, namely, solid rocket motors (SRMs). This holds true given the fact that the aforementioned propulsion concepts are relatively early in their developmental stages and have yet to surmount a plethora of technical barriers in regards to critical performance specifications.

The search for enhanced analytical models has led one to consider the mean flowfield characteristics of SRMs with tapered bores. Examples of tapered propellant surfaces can be observed in the Titan IV, Ariane, Castor, solid rocket boosters, interceptor vehicles with fast burning propellants, and other moderate size launch vehicles requiring thrust curve modifications. Most modern SRMs are manufactured with small tapers in order to facilitate the removal of the casting mandrel after the curing process has been completed. It is implied that these small tapers help to reduce the contact between the propellant surface and the mandrel, thereby reducing the possibilities of propellant tear, cracking and debonding. Additional tapering of propellant bores has served two functions: (1) minimization of erosive burning and (2) implementation of boost-sustain motor configurations. It is also speculated that tapering or coning of the propellant surfaces can help to maximize the volumetric loading fraction by increasing the port-to-throat area ratio.

Aside from the three-dimensional internal ballistics codes such as the Standard Stability Prediction[33] and the Solid Propellant Performance,[2-4] there are many industrial codes that still refer to parallel profiles (such as Culick's[10]) as a basis for design and analysis.[34] When parallel profiles are applied to tapered SRMs, the result is over-prediction of the pressure drop by as much as 50% to 85% for taper angles as small as 1°. Being in excess of 25%, such a discrepancy can drastically alter motor case design requirements to the extent of compromising the structural integrity of the motor components.

II. Mathematical Model

For academic reasons, the SRM is characterized as a cylindrical, circular-port duct with a circumferential porous surface oriented at an angle α. The model presented here in Fig. 1a incorporates both the non-tapered and tapered geometries. This allows one to account for the bulk flow originating from the non-tapered section of the motor. Here, the origin for the coordinate system is placed at the interface where $\bar{z}$ and $\bar{r}$ denote the axial and radial coordinates, respectively (see Fig. 1b). The non-tapered section of the cylindrical motor has dimensions of length L_0 and radius R_0. The gases are injected perpendicularly to the tapered burning surface. In order to satisfy mass conservation, the injected gases are forced to turn and merge with the bulk flow that originates in the parallel segment of the motor. The streamline behavior can be seen in Fig. 1a.

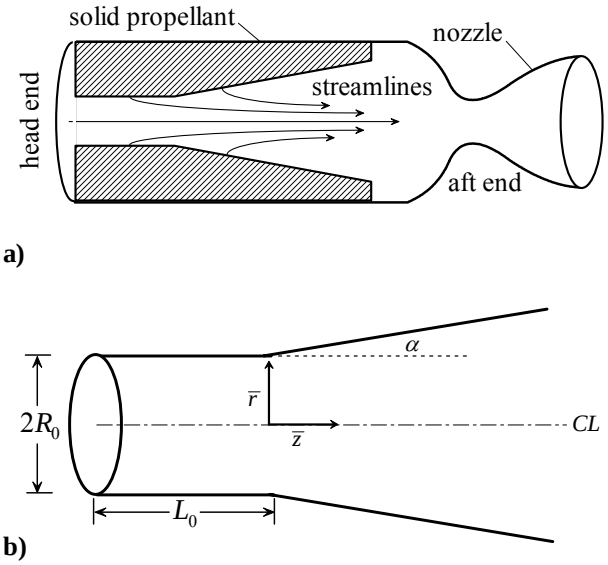

Fig. 1 Schematic featuring a) typical cylindrical solid rocket motor with tapered bore and characteristic streamlines; and b) coordinate system for the mathematical model.

A. Governing Equations

Since the vorticity is produced at the surface as a result of the interaction between the injected fluid and the axial pressure gradient, one may begin by obtaining the required form of the vorticity. Further, the flow can be characterized as (i) axisymmetric, (ii) inviscid, (iii) incompressible, (iv) rotational, and (v) non-reactive. In accordance with the stated assumptions, the kinematic equations of motion can be written in vector and scalar notations. In the interest of clarity, these are:

$$\bar{\boldsymbol{u}} \cdot \bar{\nabla} \boldsymbol{u} = -\bar{\nabla} \bar{p} / \rho \tag{1}$$

$$-\bar{\boldsymbol{\Omega}}_\theta = \bar{\nabla}^2 \bar{\psi} \tag{2}$$

$$\bar{u}_z \frac{\partial \bar{u}_r}{\partial \bar{z}} + \bar{u}_r \frac{\partial \bar{u}_r}{\partial \bar{r}} = -\frac{1}{\bar{\rho}} \frac{\partial \bar{p}}{\partial \bar{r}} \tag{3}$$

$$\bar{u}_z \frac{\partial \bar{u}_z}{\partial \bar{z}} + \bar{u}_r \frac{\partial \bar{u}_z}{\partial \bar{r}} = -\frac{1}{\bar{\rho}} \frac{\partial \bar{p}}{\partial \bar{z}} \tag{4}$$

$$-\bar{\Omega}_\theta = \frac{1}{\bar{r}} \frac{\partial^2 \bar{\psi}}{\partial \bar{z}^2} + \frac{\partial}{\partial \bar{r}} \left(\frac{1}{\bar{r}} \frac{\partial \bar{\psi}}{\partial \bar{r}} \right) \tag{5}$$

B. Boundary Conditions

While it is apparent that a radial component does exist at the interface, one should note that it does not contribute to the mass crossing into the tapered region; hence, it is not required to obtain a solution (see Fig. 2). The key constraints consist of: (i) the axial inflow condition arising from mass balance across the taper interface (accounting for the bulk flow from the parallel portion of the motor); (ii) no flow across the centerline (axisymmetry); and (iii) uniform, constant, normal injection at the burning surface. Mathematically, the boundary conditions can be evaluated and expressed in cylindrical coordinates. They give:

$$\begin{cases} \bar{z} = 0, \ \forall \bar{r}, \ \bar{u}_z = V_b \left(L_0 / R_0 \right) \pi \cos\left(\frac{1}{2} \pi r^2 / R_0^2 \right) \\ \bar{r} = \bar{r}_s, \ \forall \bar{z}, \ \bar{u}_z = V_b \sin\alpha \\ \bar{r} = \bar{r}_s, \ \forall \bar{z}, \ \bar{u}_r = -V_b \cos\alpha \\ \bar{r} = 0, \ \forall \bar{z}, \ \bar{u}_r = 0 \end{cases} \tag{6}$$

where V_b is the velocity at the burning surface.

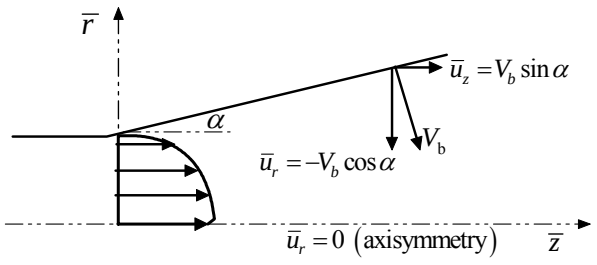

Fig. 2 Schematic of physical boundary conditions.

C. Normalization

Normalization of the variables associated with the mathematical model provides a descript and compact solution. One may set

$$z = \frac{\bar{z}}{R_0}; \ y = \frac{\bar{r}}{R_0}; L = \frac{L_0}{R_0}; \ \nabla = R_0 \bar{\nabla} \tag{7}$$

$$u_z = \frac{\bar{u}_z}{V_b}; \ u_r = \frac{\bar{u}_r}{V_b}; \ p = \frac{\bar{p}}{\rho V_b^2} \tag{8}$$

$$\psi = \frac{\bar{\psi}}{R_0 V_b}; \ \Omega = \frac{R_0 \bar{\Omega}}{V_b} \tag{9}$$

Normalizing the boundary conditions, it follows that

$$\begin{cases} z = 0, \ \forall r, \ u_z = L\pi \cos\left(\frac{1}{2} \pi r^2 \right) \\ r = r_s, \ \forall z, \ u_z = \sin\alpha \\ r = r_s, \ \forall z, \ u_r = -\cos\alpha \\ r = 0, \ \forall z, \ u_r = 0 \end{cases} \tag{10}$$

D. One-Dimensional Velocity

The geometry is based on the cylindrical coordinate system (as depicted in Fig. 3) where $\bar{z}$ is the dimensional axial coordinate and $\bar{r}$ is the dimensional radial coordinate. The area of the tapered burning surface is known to be

$$A_b = 2\pi \left(R_0 + \tfrac{1}{2} \bar{z} \tan\alpha \right) \bar{z} \sec\alpha \tag{11}$$

Also, the tapered chamber cross-sectional area is

$$A(\bar{z}) = \pi \left(R_0 + \bar{z} \tan\alpha \right)^2 \tag{12}$$

The inflow cross-sectional area at the interface of the tapered and straight portion of the chamber is given by

$$A_0 = \pi R_0^2 \tag{13}$$

As a result of a mass balance in the straight segment of the chamber, the corresponding inflow velocity becomes

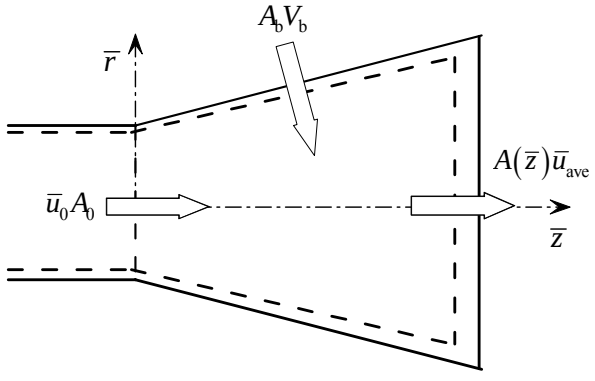

Fig. 3 Mass balance over a tapered segment.

$$\bar{u}_0 = (2L_0 / R_0)V_b \tag{14}$$

Here L_0 can be defined as the bulk flow parameter because it is directly proportional to the average velocity at the entrance to the tapered portion. Due to mass conservation, the cross-sectional average velocity of the fluid at any axial location $\bar{z}$ may be expressed by

$$\bar{u}_{ave}(\bar{z}) = \frac{A_0\bar{u}_0 + A_b V_b}{A(\bar{z})} \tag{15}$$

By substituting Eqs. (11)–(14) into Eq. (15), the average velocity becomes

$$u_{ave}(z) = 2\frac{L + z\sec\alpha\left(1 + \frac{1}{2}z\tan\alpha\right)}{\left(1 + z\tan\alpha\right)^2} \tag{16}$$

For the case $\alpha = 0$, Eq. (16) reduces to

$$u_{ave}(z) = 2(z + L) \tag{17}$$

which describes the bulk flow in a straight circular-port motor. To determine the behavior of the gases when sufficiently removed from the head end, one may manipulate Eq. (16) and compute the limit of the resulting expression. One gets

$$u_{ave}(z) = 2\left(\frac{1}{z} + \tan\alpha\right)^{-2}\left[\frac{L}{z} + \sec\alpha\left(\frac{1}{z} + \frac{1}{2}\tan\alpha\right)\right] \tag{18}$$

The limit at $z \to \infty$ furnishes

$$\lim_{z\to\infty} u_{ave}(z) = \frac{1}{\sin\alpha} \tag{19}$$

From Eq. (19), it can be seen that the velocity in a tapered chamber converges to a constant value as the motor length approaches infinity. This behavior is also illustrated in Fig. 4. Thus, it can be deduced that the flow does not continue to accelerate due to an increase in cross-sectional area that is open to the flow. This is unlike the case of a parallel port motor, where the velocity continues to increase. Typically, combined motor configurations have a parallel segment immediately followed by a tapered segment. In light of this, it is physically impossible for the velocity of the gases to increase beyond the limiting value as prescribed by the tapered geometry of the following segment. Essentially, mass conservation requires that the average velocity throughout the parallel segment of the motor remains less than or equal to the limiting value. This is equivalent to setting

$$u_{ave}(z)\big|_{\alpha=0^\circ} \le u_{ave}(\infty) \;\Rightarrow\; 2(z + L) \le \frac{1}{\sin\alpha} \tag{20}$$

With subsequent manipulation and expressing Eq. (20) in dimensional variables, one obtains

$$\frac{\alpha(L_0 + z)}{R_0} \le \frac{1}{2} \tag{21}$$

where $\alpha \approx \sin\alpha$. The geometric parameters of the motors must be chosen such that the relationship shown in Eq. (21) is satisfied. Compliance with this criterion ensures a valid solution.

E. Stream Function along the Burning Surface

A crucial component to the formulation of the flowfield under study is the development of the stream function at the simulated burning surface. It is clear that the behavior of the stream function depends on the angular orientation of the propellant surface. As a result, the directional derivative assumes the form

$$\frac{d\psi_s}{ds} = \frac{\partial\psi}{\partial z}\cos\alpha + \frac{\partial\psi}{\partial r}\sin\alpha \tag{22}$$

As shown in Fig. 5, the normalized variables along the burning surface can be readily determined to be

$$z = s\cos\alpha \tag{23}$$

$$r_s = 1 + s\sin\alpha \tag{24}$$

$$u_z = \sin\alpha \tag{25}$$

$$u_r = -\cos\alpha \tag{26}$$

The stream function relations at the simulated burning surface can be defined as

$$u_z = -\frac{1}{r}\frac{\partial\psi}{\partial r}, \quad u_r = \frac{1}{r}\frac{\partial\psi}{\partial z} \tag{27}$$

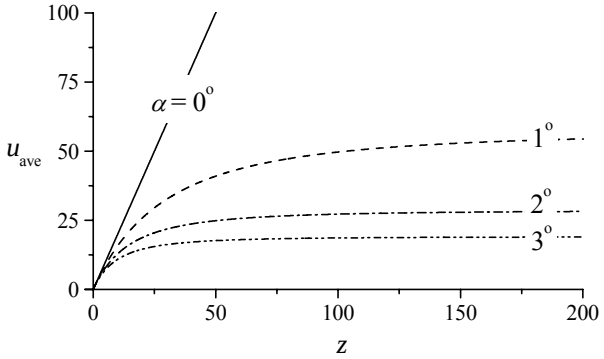

Fig. 4 Axial variation of average velocity for *L* = 0.

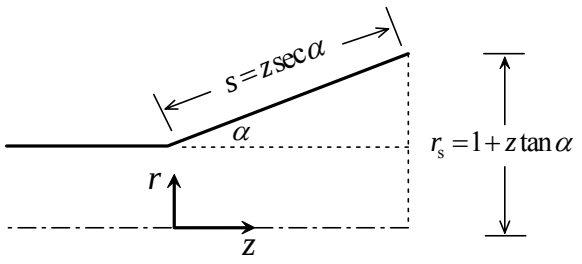

Fig. 5 Schematic of burning surface quantities.

Insertion of the stream function definitions into Eq. (22) yields

$$\frac{\mathrm{d}\psi_\mathrm{s}}{\mathrm{d}s} = -r\left(\cos^2\alpha + \sin^2\alpha\right) \Rightarrow \frac{\mathrm{d}\psi_\mathrm{s}}{\mathrm{d}s} = -\left(1 + s\sin\alpha\right) \quad (28)$$

Subsequent integration and conversion of Eq. (28) back to spatial coordinates yields $\psi_\mathrm{s}(s) = -\left(s + \frac{1}{2}s^2\sin\alpha\right)$, hence

$$\psi_\mathrm{s}(z) = -z\sec\alpha\left(1 + \tfrac{1}{2}z\tan\alpha\right) + C \quad (29)$$

where C is a constant that can be evaluated by applying the boundary condition, $\psi_\mathrm{s}(0) = -L$. Application of this constraint gives

$$\psi_\mathrm{s}(z) = -z\sec\alpha\left(1 + \tfrac{1}{2}z\tan\alpha\right) - L \quad (30)$$

F. Axial Pressure Gradient

The axial pressure gradient is deemed to be the primary source of vorticity. As a result, we may begin by expressing the axial variation of pressure in the form of Bernoulli's equation as

$$p(z) = p_0 - \tfrac{1}{2}u_\mathrm{max}^2(z) \quad (31)$$

At this juncture, it is necessary to recall that the pressure variation is sensitive to the shape of the axial velocity profile. One should also note that the shape of the profile changes at each axial location and that the maximum velocity is unknown. It is helpful to define an expression that captures the shape of the axial profile at any location z as the gases make their way toward the nozzle inlet. In that vein, we define the ratio of maximum to average velocities as

$$\beta(z) = \frac{u_\mathrm{max}(z)}{u_\mathrm{ave}(z)} \quad (32)$$

The form of $\beta(z)$ will be later determined from imposition of the no-slip requirement at the burning surface. By substituting Eq. (32) into Eq. (31), one is left with

$$p(z) = p_0 - \tfrac{1}{2}\beta^2 u_\mathrm{ave}^2(z) \quad (33)$$

The pressure gradient is determined along the simulated burning surface by evaluating the derivative of Eq. (33). The result is

$$\frac{\mathrm{d}p}{\mathrm{d}z} = -\beta^2(z)u_\mathrm{ave}(z)\left[\frac{\mathrm{d}u_\mathrm{ave}(z)}{\mathrm{d}z} + \frac{u_\mathrm{ave}(z)}{\beta(z)}\frac{\mathrm{d}\beta(z)}{\mathrm{d}z}\right] \quad (34)$$

Differentiating Eq. (16) and substituting the known surface quantities furnishes

$$\frac{\mathrm{d}u_\mathrm{ave}}{\mathrm{d}z} = 2\frac{\sec\alpha}{r_\mathrm{s}} + 4\frac{\psi_\mathrm{s}\tan\alpha}{r_\mathrm{s}^3} \quad (35)$$

Substituting Eq. (35) into Eq. (34) and simplifying, it follows that

$$\frac{\mathrm{d}p}{\mathrm{d}z} = 4\beta^2\frac{\psi_\mathrm{s}\sec\alpha}{r_\mathrm{s}^3}\left[1 + 2\frac{\psi_\mathrm{s}\sin\alpha}{r_\mathrm{s}^2} - \frac{\psi_\mathrm{s}\cos\alpha}{r_\mathrm{s}}\left(\frac{\beta'}{\beta}\right)\right] \quad (36)$$

where

$$\beta' = \frac{\mathrm{d}\beta}{\mathrm{d}z} \quad (37)$$

G. Surface Vorticity

Having determined the relationship between chamber vorticity and pressure, the momentum equation for steady, inviscid flows may be evaluated at the surface. To begin, one may recall the normalized form of Euler's equation

$$\boldsymbol{u}\cdot\nabla\boldsymbol{u} = -\nabla p/\rho \quad (38)$$

With some rearrangement, the momentum equation can be expressed in terms of the vorticity. This classic form is given by

$$\boldsymbol{u}\times\boldsymbol{\Omega} = \nabla\left(p + \tfrac{1}{2}\boldsymbol{u}\cdot\boldsymbol{u}\right) \quad (39)$$

The normalized velocity vector at the simulated burning surface can be expressed in terms of the taper angle via

$$\boldsymbol{u} = \sin\alpha\hat{\boldsymbol{i}} - \cos\alpha\hat{\boldsymbol{j}} \quad (40)$$

Evaluating the expression at the surface by substitution of Eq. (40) into (39) gives

$$\boldsymbol{u}\times\boldsymbol{\Omega} = -\Omega_\mathrm{s}\left[\sin\alpha\hat{\boldsymbol{i}} - \cos\alpha\hat{\boldsymbol{j}}\right] = -\Omega_\mathrm{s}\hat{\boldsymbol{s}} \quad (41)$$

Here $\hat{\boldsymbol{s}}$ represents the unit vector parallel to the burning surface. Accordingly, the pressure gradient along the burning surface can be expressed as

$$\frac{\mathrm{d}p}{\mathrm{d}s}\hat{\boldsymbol{s}} = \left[\frac{\mathrm{d}p}{\mathrm{d}z}\cos\alpha + \frac{\mathrm{d}p}{\mathrm{d}r}\sin\alpha\right]\hat{\boldsymbol{s}} \quad (42)$$

Equating the expressions provided by Eqs. (41) and (42) yields

$$\Omega_\mathrm{s} = -\frac{\mathrm{d}p}{\mathrm{d}z}\cos\alpha - \frac{\mathrm{d}p}{\mathrm{d}r}\sin\alpha \quad (43)$$

With values of α between 1° and 3°, the term containing $\sin\alpha$ may be neglected. Naturally, Eq. (43) can be reduced to

$$\Omega_\mathrm{s} = -\frac{\mathrm{d}p}{\mathrm{d}z}\cos\alpha + O\left(\alpha V_\mathrm{b}^2\right) \quad (44)$$

Finally, the surface vorticity can be expressed as

$$\Omega_\mathrm{s} = -4\beta^2\frac{\psi_\mathrm{s}}{r_\mathrm{s}^3}\left[1 + 2\frac{\psi_\mathrm{s}\sin\alpha}{r_\mathrm{s}^2} - \frac{\psi_\mathrm{s}\cos\alpha}{r_\mathrm{s}}\left(\frac{\beta'}{\beta}\right)\right] \quad (45)$$

The realization that no sources are present within the domain of interest enables us to invoke Crocco's known

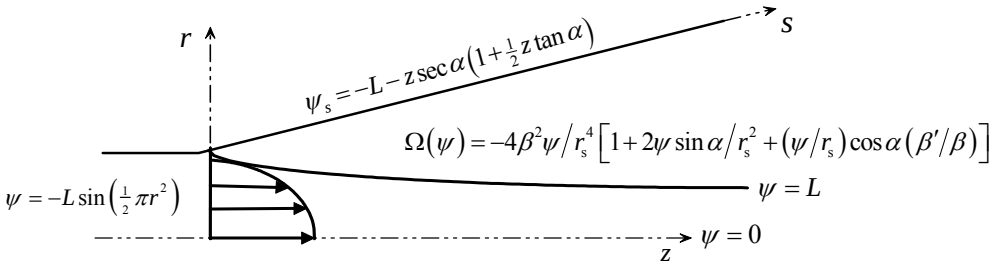

Fig. 6 Mathematical model depicting surface vorticity and stream function quantities.

theorem according to which it will be sufficient to determine vorticity along the boundaries. In the absence of sources and frictional losses, the vorticity traveling along a (steady) streamline cannot be attenuated (see Fig. 6). It remains constant along a streamline and, therefore, throughout the chamber. This mechanism is captured by Eq. (45) and will be examined further in forthcoming sections to substantiate the form of the vorticity as well as the relationship between the surface and chamber vorticity. By equating the chamber vorticity to the surface vorticity, the following expression is obtained

$$\Omega(\psi, r) = \frac{r}{r_s}\Omega_s(\psi) \tag{46}$$

Substituting Eq. (45) into (46) yields

$$\Omega(z,r) = -4\beta^2 r\frac{\psi}{r_s^4}\left[1+2\frac{\psi\sin\alpha}{r_s^2}-\frac{\psi\cos\alpha}{r_s}\left(\frac{\beta'}{\beta}\right)\right] \tag{47}$$

III. Approximate Solutions

With a complete formulation for the chamber vorticity, a partial, nonlinear equation that governs the flow is now at hand. One should note that the subscript 's' is no longer retained now that an expression that is valid for the complete chamber has been developed. One may recall that

$$\frac{\partial^2\psi}{\partial z^2}+\frac{\partial^2\psi}{\partial r^2}-\frac{1}{r}\frac{\partial\psi}{\partial r} = -4\beta^2 r^2\frac{\psi}{r_s^4}\left[1+2\frac{\psi\sin\alpha}{r_s^2}-\frac{\psi\cos\alpha}{r_s}\left(\frac{\beta'}{\beta}\right)\right] \tag{48}$$

The boundary conditions required to solve Eq. (48) are given by

$$\psi(z,0) = 0, \quad \psi(z,r_s) = \psi_s \tag{49}$$

By numerical methods, Clayton[34] noted that β' and $\partial^2\psi/\partial z^2$ were small quantities. Clayton's observations may be verified using a scaling analysis. Considering that

$$\frac{\partial^2\psi}{\partial z^2} = \frac{\partial(ru_r)}{\partial z} \tag{50}$$

one may recall that u_r is independent of z in the straight circular-port, thus causing Eq. (50) to vanish at leading order. It is clear that the presence of small taper will not affect the size of this term, given the magnitude of $\sin\alpha$. Henceforth, it is posited that the axial derivatives are of small magnitude and can be neglected in the prescribed tapered domain. Furthermore, a scaling analysis will be employed once more to verify the magnitude of β'. Using Clayton's arguments regarding the numerical analysis, Eq. (48) can be reduced to

$$\frac{\partial^2\psi}{\partial r^2}-\frac{1}{r}\frac{\partial\psi}{\partial r} = -4\beta^2 r^2\frac{\psi}{r_s^4}\left(1+2\frac{\psi\sin\alpha}{r_s^2}\right) \tag{51}$$

With a nonlinear partial differential equation at hand, the method of regular perturbations can be applied. In concert with such a methodology, the stream function and velocities may be expanded in the form

$$\psi = \psi_0 + \psi_1\varepsilon + O(\varepsilon^2) \tag{52}$$

$$u_s = u_{s,0} + u_{s,1}\varepsilon + O(\varepsilon^2) \tag{53}$$

$$\beta = \beta_0 + \psi_s\beta_1\varepsilon + O(\varepsilon^2) \tag{54}$$

where the perturbation parameter is due to the small taper angle, namely,

$$\varepsilon = \sin(\alpha) \tag{55}$$

A solution may now be obtained by the substitution of Eq. (52) and Eq. (54) into Eq. (51). The resulting expression may then be expanded into a linear sequence of ordinary differential equations.

A. Leading-Order Solution

At leading order, one obtains

$$\frac{d^2\psi_0}{dr^2}-\frac{1}{r}\frac{d\psi_0}{dr}+\frac{\beta_0^2 r^2\psi_0}{r_s^4} = 0 \tag{56}$$

which is a simple, second-order, linear differential equation with the general solution

$$\psi_0(r) = C_1 \cos\left(\beta_0 \frac{r^2}{r_s^2}\right) + C_2 \sin\left(\beta_0 \frac{r^2}{r_s^2}\right) \quad (57)$$

Straightforward evaluation of Eq. (57) at the assigned boundary conditions gives

$$\psi_0(r) = \psi_s \sin\left(\beta_0 \frac{r^2}{r_s^2}\right) \quad (58)$$

where

$$\psi_s = -\left(z \sec\alpha + \tfrac{1}{2}\varepsilon \sec^2\alpha + L\right) \text{ and } \beta_0 = \tfrac{1}{2}\pi \quad (59)$$

It should be noted that at $L = \alpha = 0$, one recovers

$$\psi_0(z,r) = z \sin\left(\beta_0 r^2\right) \quad (60)$$

Equation (60) reproduces Culick's profile[10] for flow in porous, cylindrical ducts. The leading-order solution expressed by Eq. (58) is referred to as an extended version of the Culick profile. This form is a result of the additional bulk flow produced from the extended burn area due to the angular divergence of the propellant cross section in the downstream direction.

B. First-Order Solution

At first order, one obtains the following ordinary differential equation

$$\frac{\mathrm{d}^2\psi_1}{\mathrm{d}r^2} - \frac{1}{r}\frac{\mathrm{d}\psi_1}{\mathrm{d}r} + \frac{\beta_0^2 r^2 \psi_1}{r_s^4} + \cdots$$

$$\frac{8r^2\beta_0\beta_1\psi_s\psi_0}{r_s^4} + \frac{8r^2\beta_0^2\psi_0^2}{r_s^6} = 0 \quad (61)$$

with

$$\psi_1(0) = 0, \quad \psi_1(r_s) = 0 \quad (62)$$

Applying these boundary conditions, one obtains

$$\psi_1(z,r) = \frac{\psi_s^2}{6r_s^2}\left[6 - 8\cos\left(\beta_0 \frac{r^2}{r_s^2}\right) + \cdots\right.$$

$$\left. + \cos\left(2\beta_0 \frac{r^2}{r_s^2}\right) - 4\sin\left(\beta_0 \frac{r^2}{r_s^2}\right) + 6r^2\beta_1 \cos\left(\beta_0 \frac{r^2}{r_s^2}\right)\right] \quad (63)$$

The first-order velocity ratio, β_1, must be determined such that the no-slip condition is satisfied along the tapered surface. The corresponding surface velocity may be expressed as

$$u_s = u_{z,s}\cos\alpha - u_{r,s}\sin\alpha \quad (64)$$

therefore,

$$u_s = \frac{\partial\psi}{\partial r}\cos(\alpha) + \frac{\partial\psi}{\partial z}\sin(\alpha)$$

$$= \left(\psi_0 + \psi_1\varepsilon\right)_r \cos(\alpha) + \left(\psi_0 + \psi_1\varepsilon\right)_z \sin(\alpha) \quad (65)$$

Noting that ψ_0 already satsifies the no-slip condition at the wall, the first-order surface velocity may be written as

$$u_{s,1} = \frac{\partial\psi_1}{\partial r}\cos(\alpha) + \frac{\partial\psi_1}{\partial z}\sin(\alpha) \quad (66)$$

Again, it can be seen that the term containing $\sin\alpha$ is negligibly small, being of $O(\varepsilon)$. Setting Eq. (66) equal to zero and evaluating the resulting expression at the tapered surface, one obtains

$$\beta_1 = \frac{4}{3r_s^2} \quad (67)$$

The required forms of the leading and first-order velocity ratios, β_0 and β_1, are presently known. Here, one may use a scaling analysis to justify neglecting their derivatives. Expressing the expanded velocity ratio in the form of its derivative, it is clear that

$$\beta_s' = \beta_0' + \psi_s'\beta_1'\varepsilon + O\left(\varepsilon^2\right) \quad (68)$$

With the known values of the velocity ratios, it is seen that

$$\beta_s' = \tfrac{2}{3}\sin\alpha\left(\psi_s / y_s\right)' \quad (69)$$

Evaluation of the derivative yields

$$\beta_s' = -\tfrac{4}{3}\left(1 + z\tan\alpha\right)^{-3}\frac{\sin^2\alpha}{\cos^2\alpha} \approx O\left(\varepsilon^2\right) \quad (70)$$

As seen in Eq. (70), β_1 is of order $\sin^2\alpha$. This result justifies our original premise and confirms the numerical prediction by Clayton.[34]

C. Method of Variation of Parameters

Aside from the perturbation approach, another approximate solution may be sought with the use of variation of parameters. To begin, one may recall the governing equation for tapered flow

$$\frac{\partial^2\psi}{\partial z^2} + \frac{\partial^2\psi}{\partial r^2} - \frac{1}{r}\frac{\partial\psi}{\partial r} =$$

$$-4\beta^2 r\frac{\psi}{r_s^4}\left[1 + 2\frac{\psi\sin\alpha}{r_s^2} - \frac{\psi\cos\alpha}{r_s}\left(\frac{\beta'}{\beta}\right)\right] \quad (71)$$

This may be reduced to obtain

$$\frac{\partial^2\psi}{\partial z^2} + \frac{\partial^2\psi}{\partial r^2} - \frac{1}{r}\frac{\partial\psi}{\partial r} + 4\beta^2 r^2\frac{\psi}{r_s^4} = 0 \quad (72)$$

Clearly, the most general solution assumes the form

$$\psi(z,r) = C_1(z)\sin\left(\beta\frac{r^2}{r_s^2}\right) + C_2(z)\cos\left(\beta\frac{r^2}{r_s^2}\right) \quad (73)$$

Inserting Eq. (73) into (72), one may write

$$\psi(z,r) = (K_1 z + K_2)\sin\left(\beta\frac{r^2}{r_s^2}\right) + (K_3 z + K_4)\cos\left(\beta\frac{r^2}{r_s^2}\right) \tag{74}$$

The boundary conditions at the simulated burning surface can be ascertained by evaluating the stream function at the surface. For the idealized circular-port motor with tapered bore, one has

$$\psi_s(z) = -z\sec\alpha\left(1+\tfrac{1}{2}z\tan\alpha\right) - L \tag{75}$$

Applying the definition of the stream function, one secures

$$u_z = -\frac{1}{r_s}\frac{\partial\psi_s(z,r_s)}{\partial r}\bigg|_{\forall z} = 0 \tag{76}$$

$$u_r = \frac{1}{r_s}\frac{\partial\psi_s(z,r_s)}{\partial z}\bigg|_{\forall z} = -\sec\alpha \tag{77}$$

The inflow condition is determined by a mass balance at the interface. This condition includes the bulk flow parameter and is expressed mathematically as

$$u_z = -\frac{1}{r_s}\frac{\partial\psi_s(0,r_s)}{\partial r}\bigg|_{\forall r} = -L\pi\cos\left(\tfrac{1}{2}\pi r^2\right) \tag{78}$$

The final boundary condition requires no flow across the centerline. It is also known as the condition for axisymmetry. As usual, we express this condition as

$$u_r = -\frac{1}{r_s}\frac{\partial\psi_s(z,0)}{\partial z}\bigg|_{\forall z} = 0 \tag{79}$$

With an available general solution and required boundary conditions, a particular solution may be sought. Initially, it may be observed that the condition for axisymmetry reduces the general solution to

$$\psi(z,r) = (K_1 z + K_2)\sin\left(\beta\frac{r^2}{r_s^2}\right) \tag{80}$$

Next, the no-slip condition at the simulated burning surface can be applied to render

$$u_z = -\frac{1}{r_s}\frac{\partial\psi_s(z,r_s)}{\partial r}\bigg|_{\forall z} = 0 \tag{81}$$

hence

$$\cos(\beta) = 0 \Rightarrow \beta = (2n+1)\tfrac{\pi}{2},\ n = 0 \tag{82}$$

For uniform, normal injection at the simulated burning surface, one gets

$$u_r = \frac{1}{r_s}\frac{\partial\psi_s(z,r_s)}{\partial z}\bigg|_{\forall z} = \sec\alpha \tag{83}$$

or

$$K_1\sin\left(\tfrac{1}{2}\pi\right) = \sec\alpha;\quad K_1 = \sec\alpha \tag{84}$$

The final constant of integration is determined by applying the bulk flow condition at the cylinder-taper interface ($z = 0$). Doing so, one finds

$$-K_2\frac{\pi}{r_s^3}\cos\left(\frac{\pi r^2}{2r_s^2}\right) = -L\pi\cos\left(\tfrac{1}{2}\pi r^2\right);\quad K_2 = L \tag{85}$$

Finally, the particular solution becomes

$$\psi(z,r) = (z\sec\alpha + L)\sin\left(\beta\frac{r^2}{r_s^2}\right) \tag{86}$$

It is gratifying to note that, despite the disparities in approaching this problem, the solution garnered by the variation of parameters technique begets a final expression that is identical to the leading-order solution furnished by the method of regular perturbations.

D. Velocity, Pressure and Vorticity

With the proper form of the stream function available, it is now possible to evaluate the physical characteristics of the flowfield. Since the variation of the chamber radius is of $O(\sin\alpha)$, r_s is treated as a constant for purposes of obtaining the quantities necessary to characterize the flow. Using the relationship between the velocity and stream function, the leading and first-order axial velocity profiles are expressed by

$$u_{z,0} = \frac{2\beta_0\psi_s}{r_s^2}\cos\left(\beta_0\frac{r^2}{r_s^2}\right) \tag{87}$$

and

$$u_{z,1} = \frac{\psi_s^2}{6r_s^4}\left[8\beta_0\cos\left(\beta_0\frac{r^2}{r_s^2}\right) - 16\beta_0\sin\left(\beta_0\frac{r^2}{r_s^2}\right)\right.$$
$$+8\beta_0\sin\left(2\beta_0\frac{r^2}{r_s^2}\right) - 12\beta_1\cos\left(\beta_0\frac{r^2}{r_s^2}\right)$$
$$\left.+12\beta_0\beta_1 r^2\sin\left(\beta_0\frac{r^2}{r_s^2}\right)\right] \tag{88}$$

Following suit, the leading-order radial velocity can be expressed as

$$u_{r,1} = -\frac{r_s\sec^2\alpha}{r}\sin\left(\beta_0\frac{r^2}{r_s^2}\right) + O(\varepsilon) \tag{89}$$

From the velocity profiles, the spatial variation of the pressure can be ascertained. The substitution of the velocity components into the z- and r-momentum equations yields

$$-\frac{\partial p}{\partial z} = \frac{4\beta_0^2\psi_s}{r_s^4}\sec\alpha \tag{90}$$

and

$$-\frac{\partial p}{\partial r}=\frac{1}{r^3 r_s^2}\left\{\sec^2\alpha\sin\left(\beta_0\frac{r^2}{r_s^2}\right)\right.$$
$$\left.\left[-r_s^4\sin\left(\beta_0\frac{r^2}{r_s^2}\right)+r^2\beta_0\cos\left(\beta_0\frac{r^2}{r_s^2}\right)\right]\right\} \qquad (91)$$

By integrating and combining Eqs. (90) and (91), one is able to produce the spatial variation of the pressure that satisfies both momentum equations. By inspection, one comes to the conclusion that the radial component of pressure is of marginal importance, being of $O(\sin^2\alpha)$. At leading order, Eq. (90) may be integrated to obtain

$$-p(z)=\frac{4\beta_0^2\sec\alpha}{r_s^4}\left(\tfrac{1}{2}z^2\sec\alpha+Lz\right)+\text{ constant} \qquad (92)$$

One can now apply the head-end boundary condition, $p(0,0)=p_{\text{Culick}}$, where $p_{\text{Culick}}=-L^2\pi^2/2$; the constant becomes equal to p_{Culick}. Setting $\Delta p=p(z,r)-p_{\text{Culick}}$, one can express the leading-order expression for the pressure drop as

$$\Delta p_0=-\frac{4\beta_0^2\sec\alpha}{r_s^4}\left(\tfrac{1}{2}z^2\sec\alpha+Lz\right) \qquad (93)$$

Knowing that r_s is treated as a constant for first-order approximations, it may be argued that some error may be incurred as a result of performing multiple differentiation and integration operations that neglect the axial dependence of the radius. Also, the evaluation of the derivatives and subsequent integration of the resulting expression produce higher-order terms that, for purposes of exacting a leading-order solution, may be dismissed. In an attempt to recover accuracy, one may seek a higher-order correction for the pressure drop. This higher-order correction accounts for the second-order axial derivative of the stream function as well as the variation of r_s with axial distance. Evidently, this variation becomes more significant at larger taper angles. Our second-order accurate approximation for the pressure drop can be expressed as

$$\Delta p(z;\varepsilon)=-\frac{2\beta_0^2\sec^4\alpha}{r_s^4}\left[\frac{1}{4}z^4\varepsilon^2+\frac{1}{2}z^3\sin 2\alpha+\cdots\right.$$
$$\left.z^2\cos^2\alpha(1+L\varepsilon)+2Lz\cos^3\alpha\right] \qquad (94)$$

In addition to the formulation of the velocity and pressure gradients, one may evaluate the vorticity in order to complete the extraction of standard physical parameters that characterize this flowfield. This can be accomplished via

$$\Omega_\theta(z,r)=\frac{\partial u_z}{\partial r}-\frac{\partial u_r}{\partial z} \qquad (95)$$

Inserting the relations for the velocity components into Eq. (95) produces the expression for the spatial variation of chamber vorticity. One finds

$$\Omega_\theta(z,r)=\frac{1}{r}\left(\frac{\sec\alpha\tan\alpha}{r}-\frac{4r\psi_s}{r_s^4}\right)\sin\left(\beta_0\frac{r^2}{r_s^2}\right) \qquad (96)$$

Each of the required flowfield characteristics particular to tapered cylindrical motors is now at hand. The effect of the bulk flow parameter will be examined along with the taper angle. One should note that this parameter is also the normalized chamber length $L=L_0/R_0$.

E. Ideal Momentum Thrust

Of particular interest here is the behavior of the thrust at various values of the taper angle α. One may theorize that the thrust responds to the taper angle in the same manner as the pressure drop. This behavior may be ascribed to the fact that both the pressure drop and thrust produced exhibit a strong dependence on the gas velocity in the combustion chamber. In pursuit of an expression that reveals the response of the thrust to the taper angle, one may employ the momentum thrust equation given by

$$F=\frac{\partial}{\partial t}\int_{\text{cv}}\rho V\,\mathrm{d}\upsilon+\int_{\text{cs}}\rho V(\boldsymbol{V}\cdot\hat{\boldsymbol{n}})\,\mathrm{d}A \qquad (97)$$

One may also utilize the expressions for the average velocity and the chamber cross-sectional area (introduced previously) to aid in the formulation of an expression for the thrust. Specifically, one can put

$$u_{\text{ave}}=2\frac{L+z\sec\alpha(1+\frac{1}{2}z\tan\alpha)}{(1+z\tan\alpha)^2} \qquad (98)$$

$$A(z)=\pi(1+z\tan\alpha)^2 \qquad (99)$$

One should bear in mind that only the steady state solution is of interest here. Equation (97) becomes

$$F=\int_{\text{cs}}\rho V(\boldsymbol{V}\cdot\hat{\boldsymbol{n}})\,\mathrm{d}A \qquad (100)$$

The definitions of cross-sectional area and average velocity presented in Eqs. (98) and (99) can be inserted into the steady momentum thrust equation to give

$$F=4\pi\rho\left[L+z\sec\alpha(1+\tfrac{1}{2}z\tan\alpha)\right]^2\int_{z=0}^{z=L^*}\frac{\mathrm{d}(1+z\tan\alpha)}{(1+z\tan\alpha)} \qquad (101)$$

The thrust can also be expressed in terms of the burning surface quantities. Doing so, one obtains

$$F=4\pi\rho\psi_s^2\int_{z=0}^{z=L^*}\frac{\mathrm{d}r_s}{r_s} \qquad (102)$$

In pursuit of a complete formulation that gives the thrust as a function of taper angle and axial distance, Eq. (102) must be integrated along the maximum length L^* of the tapered domain. This integration yields

$$F = 4\pi\rho \ln\left(1 + L^* \tan\alpha\right)\psi_s^2 \qquad (103)$$

where $\psi_s = L + z\sec\alpha(1 + \frac{1}{2} z \tan\alpha)$ represents the stream function along the simulated burning surface.

IV. CFD Confirmation

Available analytical methods have enabled us to obtain closed-form approximations that describe the mean flowfield for the circular-port motor with tapered bore. By closely examining some of the terms, we have previously determined that they were sufficiently small to be ignored, in the hope that their associated errors would not compound. At the outset, an analytical solution was possible by both the method of regular perturbations and variation of parameters. At this juncture, a numerical simulation can be invoked to further validate the analytical results and verify their assumptions and ranges of applicability which, so far, could only be estimated with asymptotics. In the interest of simplicity, a numerical simulation will be performed with the use of a commercial code;[35] the purpose will be to recreate as much as possible the same simulated environment that was evoked in deriving the analytical solutions.

A. Geometry and Meshing Scheme

The geometric models are created for taper angles ranging from 1° to 3°. The dimensions are chosen in accordance with the parameters used by the analytical model. The cylindrical motor is modeled in three-dimensional space, and the gaseous mixture (assuming single phase) is injected across its simulated burning surface. A standard meshing scheme is employed with an interval size of 0.1.

B. Boundary and Operating Conditions

The working fluid is injected at velocities ranging from 0.1 m/s to 1 m/s. These values of injection velocity ensure that the Mach number remains less than 0.3, hence justifying the incompressible flow condition used in the analytical part. The selection of the injection velocity can be further validated from experimental work by Brown[36] and co-workers as well as a research team led by Dunlap.[37] In fact, the selected injection velocity is inspired by Clayton's CFD results based on practical industrial applications;[34] in that context, Clayton determines that the taper profiles change minimally with increasing injection velocity provided that the Reynolds number, $Re = \rho V_b D/\mu$, remains between 10^2 and 10^4. The reference pressure we use is the stagnation pressure at the head end of the chamber, specifically, the pressure at the origin.

In order to capture coherent structures that correspond to our analytical solution, the numerical scheme that we adopt is based on the laminar model. We recognize, however, that the flowfield inside an actual SRM can be turbulent, particularly, in the downstream portions of an elongated chamber; this idea is nicely described by Apte and Yang.[38]

V. Results and Discussion

This section seeks to examine the dissimilarities that exist between the numerical and analytical cases presented earlier. With available information, one is able to determine the level of accuracy that is required and which physical parameters are most important. As noted by Clayton,[34] the axial velocity profiles and the pressure drop are of paramount importance. However, the pursuit of a general expression that describes the flowfield in tapered geometry requires that certain terms be neglected during the derivation process. To validate the dismissal of these terms, the same problem is now solved numerically. In the forthcoming sections, the numerical results will be compared to those found analytically.

A. Pressure Approximations

The slow increase in cross-sectional area in the axial direction acts to decrease the pressure drop by allowing a build-up in local static pressure with the accompanying decrease in dynamic pressure. By comparison to Culick's solution in a straight circular-port motor,[10] Fig. 7a and Fig. 7b illustrate that there are substantial decreases in the pressure drop at higher taper angles taken at a length-to-radius ratio of $z = 10$. The value of z corresponds to the maximum length of the tapered segment for a bulk flow value of zero. Recovering the error that has accrued as a result of the constant radius assumption and neglecting the second-order axial derivative requires the addition of a higher-order correction.

The behavior of the higher-order solution can be examined in Fig. 7b. The addition of the higher-order correction seems to have much more of an impact at higher taper angles and larger tapered domains; this trend suggests that the corrections are a requisite for analytical pressure predictions for these cases. Compared to the higher-order solution, the leading-order solution under-predicts the pressure drop at larger taper angles. In later portions of this work, the higher-order correction will prove to be essential for the validation of the mathematical model. It is clear that there is an over-prediction in pressure drop. The error increases as the gases head toward the aft end of the

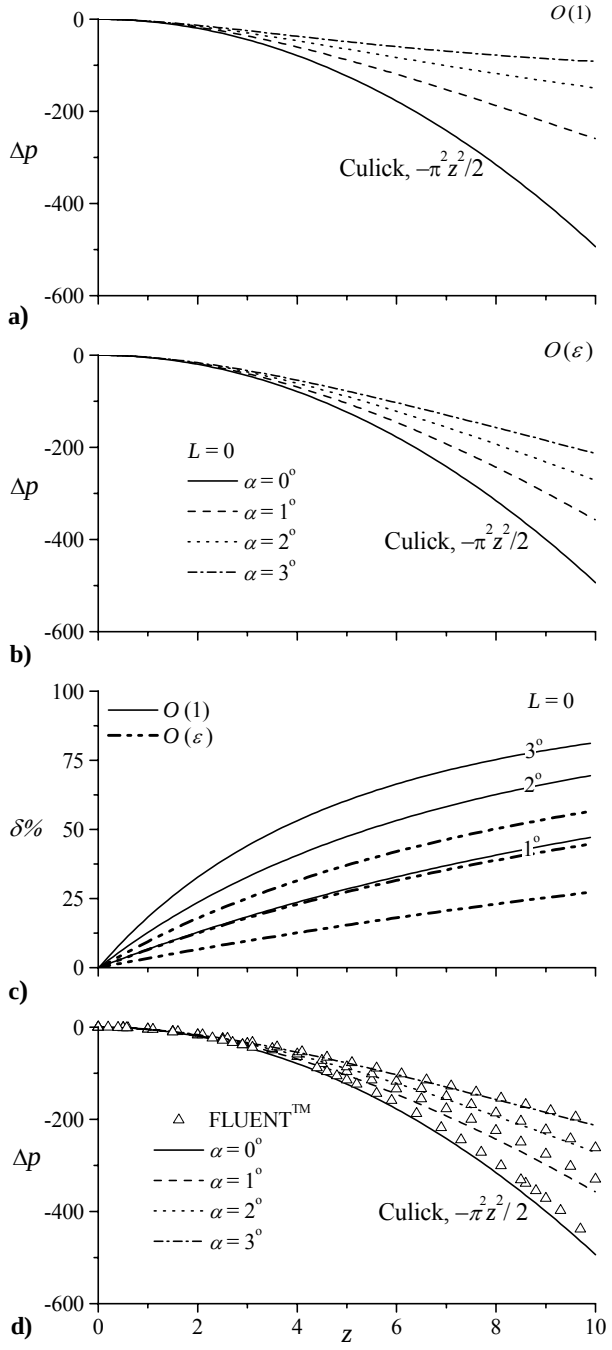

Fig. 7 Plots of a) leading order and b) first-order approximations for several values of α. In c) the percent over-prediction at several values of α and d) numerical vs. first-order approximation are shown.

motor. At the edge of the solution domain, the total pressure drop can be over-predicted by as much as 48% to 75% using the leading-order expression. The natural range for percent over-prediction using the higher-order correction varies here between 24 and 52 percent. Obviously, use of the leading-order solution to predict the total pressure drop is not acceptable.

B. Momentum Thrust Behavior

In Fig. 8, the sensitivity of idealized momentum thrust seems to be consistent with that of the pressure drop when evaluated as function of taper angle. As the area increases in the axial direction, mass continuity requires the average velocity to slow down in an effort to compensate for the change in available flow area. Accordingly, the thrust at each axial location tends to decrease as well. This trend is clearly illustrated with successive increases in α. Physically, the plot represents a steady state, cold flow solution that does not account for neutral, regressive or progressive burning effects. Also, the important nozzle effects are totally discounted. Based on this cold flow model, the simulated motor may be thought of as regressive in nature. Since the average velocity approaches a constant value, it is reasonable to theorize that the thrust may follow suit. Without accounting for the taper effect, it may be speculated that one-dimensional prediction of the thrust can lead, by analogy with the pressure drop, to a slight over-prediction that becomes more appreciable with increasing taper.

C. Axial Velocity

One should recall that r_s was treated as a constant during the evaluation of the axial and radial velocity components. Consequently, it was expected that some error would be introduced into the solution. In Fig. 9, it can be observed that there exists no discernable pattern for the analytical profiles and their numerical counterparts. This may be attributed to the effects of curvature as well as the non-uniform 3-D computational grid used for the numerical model. As a result, the numerical solution is seen to slightly overshoot or undershoot the numerical solution at various axial locations. This rather random discrepancy is more noticeable further down the motor chamber; it may

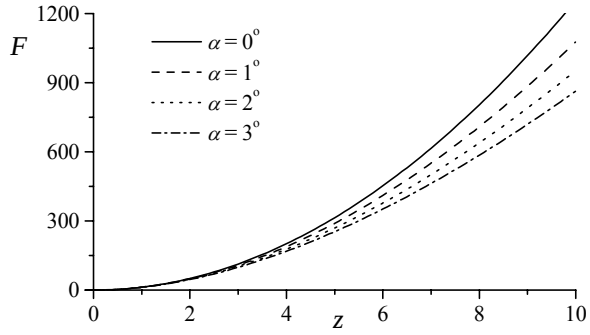

Fig. 8 Idealized momentum thrust (dimensionless) along midsection plane at several taper angles.

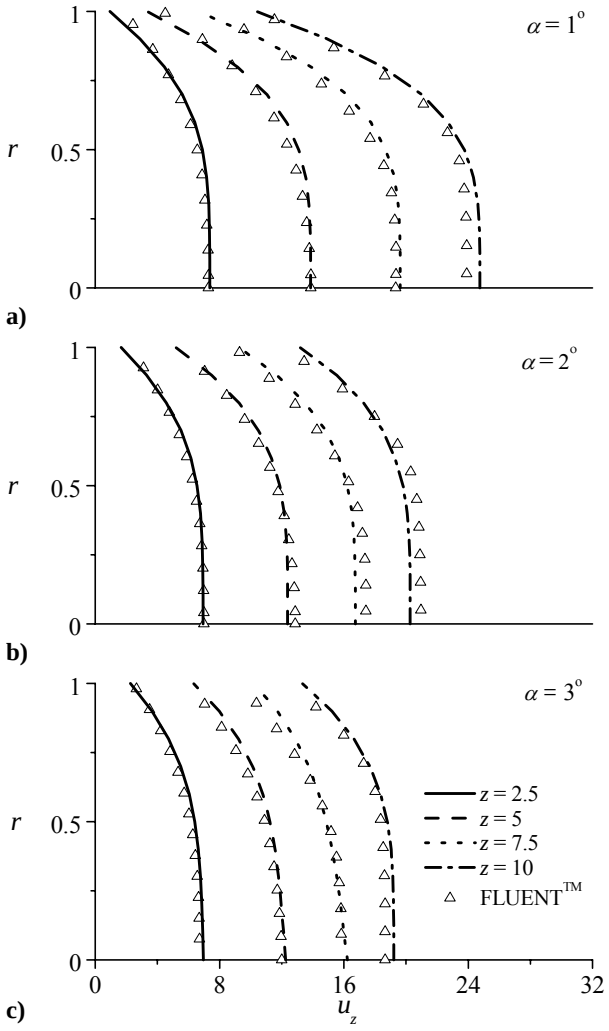

Fig. 9 CFD versus analytical velocity profiles at various axial locations for select taper angles.

become non-negligible in very long motors.

At this juncture, one should note that the analytical solutions shown in Fig. 9 include higher-order corrections. Neglecting these higher-order terms leads to a grossly under-predicted maximum centerline velocity. From the graph, it can be inferred that the leading-order solution lacks valuable flow information and that the higher-order terms appear to be a requisite for accurate solutions in long chambers with large taper angles. The higher-order corrections seem to slowly recover the second-order axial derivative that was omitted in the basic solution. Clearly, Fig. 9 displays very good agreement between the analytical and numerical solutions. This justifies the use of the analytical formula in lieu of numerical simulations in fundamental theoretical studies that require either a concrete or discretized form of the velocity field.

D. Axial Derivatives

Our quest for an analytical, closed form solution required several assumptions. These assumptions targeted several derivatives, namely: (1) $\partial^2\psi/\partial z^2$ and (2) $\mathrm{d}\beta/\mathrm{dz}$.

The magnitudes of the second-order axial derivatives of stream function have been extracted from the numerical solution and quantified along the axis. The second-order radial derivatives were also plotted for the purpose of comparing the two quantities. Figure 9a clearly depicts an oscillatory behavior as is typical of a small fluctuating quantity. These fluctuations remain insignificant, namely, of $O(10^{-4})$ down the length of the chamber. In contrast, the radial derivatives shown in Fig. 10b exhibit magnitudes of $O(1)$, thus justifying their retention in the analytical model.

Similarly, the magnitudes of the axial derivatives (described in Fig. 10c) for the velocity ratio are small

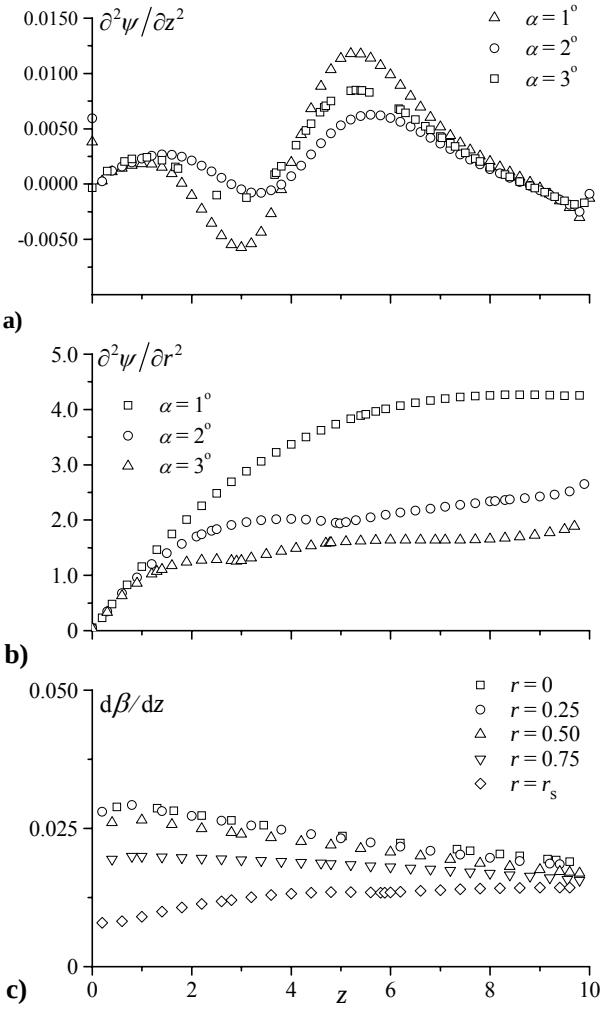

Fig. 10 Numerical axial derivative approximations from FLUENT™ shown at several taper angles.

enough that they would have no appreciable effect on the analytical solution. This plot shows the axial variation of $\mathrm{d}\beta/\mathrm{dz}$ at several radial locations for $\alpha = 3^\circ$. From the graph, it can be inferred that the axial variation of each derivative dictates the shape of the velocity profile. For example, at $r = r_s$, the axial derivative slowly increases. One may recall that the velocity profile must adjust itself at each axial location to satisfy the no-slip requirement at the tapered surface. Bearing this in mind, it can be realized that the rate of change at the wall must increase due the increased axial variation as the gases propagate down the chamber. At the axis of the chamber, one notices a decreasing derivative. This also indicates that the centerline velocity must decrease in the axial direction. From a physical standpoint, these changes must occur to satisfy mass conservation. The increasing rate of change at the wall works in conjunction with the decreasing rate of change at the axis to force the profile to slowly relinquish its radial dependence with increasing axial distance. Hence, the profile may evolve into a near constant shape over the cross-section perpendicular to the flow for sufficiently long tapered domains.

VI. Solution Limitations

For practical applications of the analytical solutions presented heretofore, one may be concerned with their parametric limitations. Previously, such limitations were explored by analytically predicting the behavior of the gases at an infinite distance away from the head end. The results of this inquiry suggest that some relationships, guided by mass conservation, must be maintained between the geometric parameters. As shown in Sec. II(D), the pertinent relationship can be expressed as:

$$\frac{\alpha\left(L_0 + \bar{z}\right)}{R_0} \le \frac{1}{2} \tag{104}$$

This criterion was obtained using the average value of the velocity as opposed to the maximum centerline velocity. In order to determine a maximum range for which the analytical solutions remain applicable, one must calculate the maximum relative error between asymptotic predictions and numerical solutions. To do so, it is expedient to examine the asymptotic limit where the velocities in each chamber are at their maximum values; this can be accomplished, for instance, by comparing the centerline velocities predicted by numerics and those by asymptotics. For the non-tapered segments, the relationship between centerline and average velocities can be easily found to be

$$u_{\max} = \tfrac{1}{2}\pi u_{\text{ave}} \tag{105}$$

By translating this result to the centerline velocity, the criteria that establish the upper limit of the solution domain may be extrapolated. One finds

$$\frac{\alpha\left(L_0 + \bar{z}\right)}{R_0} \le \frac{1}{\pi} \tag{106}$$

Equation (106) can now be solved for $L_0 = 0$ to obtain the maximum *conservative* domain aspect ratio for a given taper angle. One finds

$$z_{\text{cons}} = \frac{1}{\alpha\pi} \tag{107}$$

where $z_{\text{cons}} = \bar{z}/R_0$. It is our observation that, so long as $z \le z_{\text{cons}}$, the percent error between numerics and asymptotics remains less than 1%. The conservative range represents a domain of asymptotic validity in which the accrued error is virtually insignificant. By requiring a minimum chamber aspect ratio of 4 (lest edge effects become important), the maximum conservative taper angle for which an asymptotic solution would exhibit a smaller than 1% error can be readily calculated from Eq. (107). One finds the maximum conservative taper angle to be 4.5 degrees. Therefore, a suitable range of tapers would be $0 < \alpha \le 4.5^\circ$.

Shown in Figs. 10a and 10b are the centerline velocities for $\alpha = 1^\circ$ and 4.5°, respectively. The behavior at $\alpha = 1^\circ$ is quite similar, although the range is different (due to the difference in geometries). In Fig. 11a, it is seen that the maximum percent deviation is about 16.4%. Here, the conservative range is $0 < z \le 18.2$. As predicted, the two solutions (numerical and analytical) begin to diverge outside of the conservative domain.

For the case of the maximum taper angle, $\alpha = 4.5^\circ$, the conservative range is shrunk down to $0 < z \le 4$. The location at which there is a 20% discrepancy between the two solutions is found to be approximately 17.0. For values greater than 17.0, the deviation begins to increase until it reaches a maximum value of 42.2%. The numerical cases shown here clearly support the analytical criterion within the conservative range. It may be inferred that the analytical solution exhibits a larger range of applicability for smaller taper angles.

For the idealized circular port motor with very small taper (Fig. 11a), the maximum percent deviation, δ, is about 16.0% (at which point the error between numerics and asymptotics remains approximately constant as the solution levels off to a constant value). For such small taper, one may apply the analytical solution with minimal error, at least in theory, over an infinitely long domain. The range of aspect ratios for

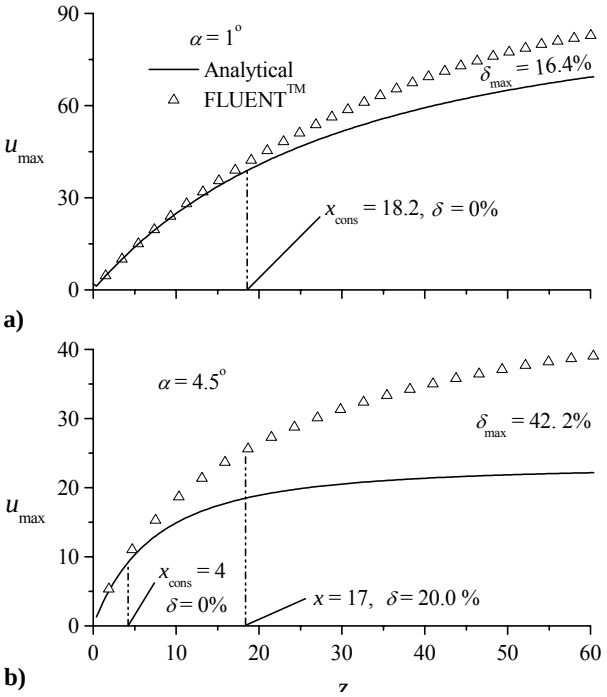

Fig. 11 Numerical and analytical approximations of the maximum (centerline) velocity with attendant relative error for two taper angles.

which relative discrepancies remain under 20% is generally much longer than those currently used in practice. For practical applications, such as cold flow models for SRMs, the solution presented in this work would consistently remain within 20% of the numerical cases up to $z/z_{cons} \cong 4$.

VII. Conclusions

In this study, we have presented approximate solutions for the mean flowfield in circular-port rocket motors with tapered bores. Analytical solutions were obtained with the use of two methods: (1) the method of regular perturbations and (2) variation of parameters. Additionally it was found that the solution from the use of variation of parameters is identical to the leading-order solution shown earlier. Although the distance from the axis to the simulated burning surface varies with axial distance, it is assumed constant in the evaluation of the velocity, vorticity and most notably, the pressure drop.

In pursuit of expressions that characterize the chamber pressure, mathematical operations were performed with the assumption that the distance from the centerline was constant, because its variation was of $O(\sin\alpha)$. In light of this, higher-order corrections were needed. Most notably, the higher-order corrections were found to compensate for the assumption of axial independence of the chamber radius. Furthermore, the higher-order corrections were able to recover the effect of the second-order axial derivative of the stream function as well as the radial and transverse expansion and flow deceleration.

In conclusion, we have demonstrated that the pressure drop is over-predicted if Culick's mean flowfield is applied to chambers with tapered bores. Evidently, this suggests the modification of ballistics codes that attempt to predict and characterize bulk gas motion without giving due attention to tapering.

Given the methodologies used throughout this work to obtain the desired flowfield, the numerical simulation has been instrumental in substantiating the assumptions demanded by the analytical derivation. Our study confirms the usefulness of numerical models in validating approximate solutions, especially those that are asymptotic in nature. Both theoretical avenues concur in that:

- The incorporation of the taper is required to avoid over-predicting the pressure drop.
- The taper effect is more pronounced as the gases move away from the head end due to the increasing cross-sectional flow area.
- Long motors with $L \geq 4$ experience reduced sensitivity to taper angle. Smaller motors experience increased sensitivity.
- The mean flow approaches its asymptotic limit in sufficiently long motors.
- When modeling short motors or those with smaller taper angles, such as $0.5^\circ < \alpha \leq 1^\circ$, the leading order solution is sufficient; however, for larger angles and longer motors, higher-order corrections are required.
- The ideal momentum thrust diminishes at higher taper angles and increases with motor length until it reaches its asymptotic limit.

In closing, it may be worth mentioning that accurate matching of both numerical and analytical solutions requires that the motor parameters be chosen within specified limits. The corresponding criteria are discussed and shown to be practical. One shortcoming in the analytical solution is that it is long, albeit simple to implement and evaluate. While the leading-order solution can be expressed concisely, it is of marginal accuracy as it only applies to motors with relatively short tapered segments and/or small taper angles. Better precision can be achieved when the higher-order corrections are utilized. In future work, we hope to extend this investigation to chambers with arbitrary cross section.

Acknowledgments

This project was partly sponsored by the Faculty Early Career Development (CAREER) Program of the National Science Foundation under Grant No. CMS-0353518. The authors wish to express their sincere gratitude to the Program Director, Dr. Masayoshi Tomizuka, Dynamic Systems and Control. His support for this project is greatly appreciated. The authors are also indebted to Dr. Curtis D. Clayton for his assistance in conducting this work.

References

[1]Sutton, G. P., *Rocket Propulsion Elements*, 6th ed., John Wiley, New York, 1992.

[2]Coats, D. E., and Dunn, S. S., "Solid Performance Program (SPP) Version 7.2 Vav," Software and Engineering Associates, Inc., SEA TR 95-021995.

[3]Nickerson, G. R., Coats, D. E., Hersmen, R. L., and Lamberty, J., "A Computer Program for the Prediction of Solid Propellant Rocket Motor Performance (SPP)," Software and Engineering Associates, Inc., AFRPL TR-83-036, CA, September 1983.

[4]Coats, D. E., and Dunn, S. S., "Improved Motor Stability Predictions for 3D Grains Using the SPP Code," AIAA Paper 97-33251, July 1997.

[5]Sabnis, J. S., Gibeling, H. J., and McDonald, H., "Navier-Stokes Analysis of Solid Propellant Rocket Motor Internal Flows," *Journal of Propulsion and Power,* Vol. 5, No. 6, 1989, pp. 657-664.

[6]Fiedler, R. A., Jiao, X., Namazifard, A., Haselbacher, A., Najjar, F. M., and Parsons, I. D., "Coupled Fluid-Structure 3-D Solid Rocket Motor Simulations," AIAA Paper 2001-3954, July 2001.

[7]Venugopal, P., Najjar, F. M., and Moser, R. D., "DNS and LES Computations of Model Solid Rocket Motors," AIAA Paper 2000-3571, July 2000.

[8]Venugopal, P., Najjar, F. M., and Moser, R. D., "Numerical Simulations of Model Solid Rocket Motor Flows," AIAA Paper 2001-3950, July 2001.

[9]Wasistho, B., Haselbacher, A., Najjar, F. M., Tafti, D., Balachandar, S., and Moser, R. D., "Direct and Large Eddy Simulations of Compressible Wall-Injection Flows in Laminar, Transitional, and Turbulent Regimes," AIAA Paper 2002-4344, July 2002.

[10]Culick, F. E. C., "Rotational Axisymmetric Mean Flow and Damping of Acoustic Waves in a Solid Propellant Rocket," *AIAA Journal,* Vol. 4, No. 8, 1966, pp. 1462-1464.

[11]Majdalani, J., and Flandro, G. A., "The Oscillatory Pipe Flow with Arbitrary Wall Injection," *Proceedings of the Royal Society, Series A,* Vol. 458, No. 2022, 2002, pp. 1621-1651.

[12]Majdalani, J., and Van Moorhem, W. K., "Improved Time-Dependent Flowfield Solution for Solid Rocket Motors," *AIAA Journal,* Vol. 36, No. 2, 1998, pp. 241-248.

[13]Majdalani, J., and Van Moorhem, W. K., "The Unsteady Boundary Layer in Solid Rocket Motors," AIAA Paper 95-2731, July 1995.

[14]Majdalani, J., Flandro, G. A., and Roh, T. S., "Convergence of Two Flowfield Models Predicting a Destabilizing Agent in Rocket Combustion," *Journal of Propulsion and Power,* Vol. 16, No. 3, 2000, pp. 492-497.

[15]Majdalani, J., Vyas, A. B., and Flandro, G. A., "Higher Mean-Flow Approximation for a Solid Rocket Motor with Radially Regressing Walls," *AIAA Journal,* Vol. 40, No. 9, 2002, pp. 1780-1788.

[16]Flandro, G. A., and Majdalani, J., "Aeroacoustic Instability in Rockets," *AIAA Journal,* Vol. 41, No. 3, 2003, pp. 485-497.

[17]Malhotra, S., and Flandro, G. A., "On the Origin of the Dc Shift," AIAA Paper 97-3249, July 1997.

[18]Flandro, G. A., Majdalani, J., and French, J. C., "Nonlinear Rocket Motor Stability Prediction: Limit Amplitude, Triggering, and Mean Pressure Shift," AIAA Paper 2004-4054, July 2004.

[19]Flandro, G. A., Majdalani, J., and Sims, J. D., "Nonlinear Longitudinal Mode Instability in Liquid Propellant Rocket Engine Preburner," AIAA Paper 2004-4162, July 2004.

[20]Féraille, T., Casalis, G., and Dupays, J., "Particle Effects on Solid-Propellant Motors Flow Stability," AIAA Paper 2002-3611, July 2002.

[21]Thomas, H. D., Flandro, G. A., and Flanagan, S. N., "Effects of Vorticity on Particle Damping," AIAA Paper 95-2736, July 1995.

[22]Rao, N. X., and Van Moorhem, W. K., "Interactions of Particles with the Flow near the Burning Surface of a Solid Propellant Rocket," AIAA Paper 93-0110, January 1993.

[23]Elgobashi, S., "On Predicting Particle-Laden Turbulent Flows," *Applied Scientific Research,* Vol. 52, 1994, p. 309.

[24]Sabnis, J. S., de Jong, F. J., and Gibeling, H. J., "Calculation of Particle Trajectories in Solid-Rocket Motors with Arbitrary Acceleration," *Journal of Propulsion and Power,* Vol. 8, No. 5, 1992, pp. 961-967.

[25]Vuillot, F., Dupays, J., Lupoglazoff, N., Basset, T., and Daniel, E., "2-D Navier-Stokes Stability Computations for Solid Rocket Motors: Rotational, Combustion and Two-Phase Flow Effects," AIAA Paper 97-3326, July 1997.

[26]Lupoglazoff, N., and Vuillot, F., "Parietal Vortex Shedding as a Cause of Instability for Long Solid Propellant Motors. Numerical Simulations and Comparisons with Firing Tests," AIAA Paper 96-0761, January 1996.

[27]Lupoglazoff, N., and Vuillot, F., "Numerical Simulations of Parietal Vortex-Shedding Phenomenon in a Cold-Flow Set-Up," AIAA Paper 98-3220, July 1998.

[28]Couton, D., Doan-Kim, S., and Vuillot, F., "Numerical Simulation of Vortex-Shedding Phenomenon in a Channel with Flow Induced through Porous Wall," *International Journal of Heat and Fluid Flow,* Vol. 18, No. 3, 1997, pp. 283-296.

[29]Griffond, J., Casalis, G., and Pineau, J.-P., "Spatial Instability of Flow in a Semiinfinite Cylinder with Fluid Injection through Its Porous Walls," *European Journal of Mechanics B/Fluids,* Vol. 19, No. 1, 2000, pp. 69-87.

[30]Casalis, G., Avalon, G., and Pineau, J.-P., "Spatial Instability of Planar Channel Flow with Fluid Injection through Porous Walls," *The Physics of Fluids,* Vol. 10, No. 10, 1998, pp. 2558-2568.

[31]Griffond, J., and Casalis, G., "On the Nonparallel Stability of the Injection Induced Two-Dimensional Taylor Flow," *The Physics of Fluids,* Vol. 13, No. 6, 2001, pp. 1635-1644.

[32]Griffond, J., and Casalis, G., "On the Dependence on the Formulation of Some Nonparallel Stability Approaches Applied to the Taylor Flow," *The Physics of Fluids,* Vol. 12, No. 2, 2000, pp. 466-468.

[33]French, J. C., Flandro, G. A., and Majdalani, J., "Improvements to the Linear Stability Prediction Program (SSP)," AIAA Paper 2004-4181, July 2004.

[34]Clayton, C. D., "Flowfields in Solid Rocket Motors with Tapered Bores," AIAA Paper 96-2643, July 1996.

[35]*Fluent UNS Theory Manual*, 6.1 ed., Fluent Inc., Palo Alto, California, 2002.

[36]Brown, R. S., Blackner, A. M., Willoughby, P. G., and Dunlap, R., "Coupling between Acoustic Velocity Oscillations and Solid Propellant Combustion," *Journal of Propulsion and Power,* Vol. 2, No. 5, 1986, pp. 428-437.

[37]Dunlap, R., Blackner, A. M., Waugh, R. C., Brown, R. S., and Willoughby, P. G., "Internal Flow Field Studies in a Simulated Cylindrical Port Rocket Chamber," *Journal of Propulsion and Power,* Vol. 6, No. 6, 1990, pp. 690-704.

[38]Apte, S., and Yang, V., "Effect of Acoustic Oscillation on Flow Development in a Simulated Nozzleless Rocket Motor," *Solid Propellant Chemistry, Combustion, and Motor Interior Ballistics*, Vol. 185, edited by V. Yang, T. B. Brill, and W.-Z. Ren, AIAA Progress in Astronautics and Aeronautics, Washington, DC, 2000, pp. 791-822.